Holographic study on QCD phase transition and phase diagram with two flavors

Xin-Yi Liu[*]

Department of Applied Physics, School of Physics and Electronics, Hunan University,
Changsha 410082, China
and School of Fundamental Physics and Mathematical Sciences, Hangzhou Institute for Advanced Study,
UCAS, Hangzhou 310024, China

Xiao-Chang Peng[†]

Department of Applied Physics, School of Physics and Electronics, Hunan University,
Changsha 410082, China

Yue-Liang Wu[‡]

School of Physical Sciences, University of Chinese Academy of Sciences, Beijing 100049, China;
CAS Key Laboratory of Theoretical Physics, Institute of Theoretical Physics,
Chinese Academy of Sciences, Beijing 100190, China;
and International Centre for Theoretical Physics Asia-Pacific (ICTP-AP),
University of Chinese Academy of Sciences, Beijing 100049, China

Zhen Fang[§]

Department of Applied Physics, School of Physics and Electronics, Hunan University,
Changsha 410082, China
and Hunan Provincial Key Laboratory of High-Energy Scale Physics and Applications,
Hunan University, Changsha 410082, China

We investigate the chemical potential effects of the equation of state and the chiral transition in an Einstein-Maxwell-dilaton-scalar system, which is obtained from an improved soft-wall anti–de Sitter/QCD model coupled with an Einstein-Maxwell-dilaton system. The equations of state obtained from the model are in quantitative agreement with the lattice results at both zero and nonzero chemical potentials. The sensible chiral transition behaviors can be realized in the model. The QCD phase diagram with a critical end point has also been obtained from the model.

I. INTRODUCTION

The investigations of quantum chromodynamics (QCD) phase transition and the construction of the QCD phase diagram are of paramount importance in the field of theoretical physics. These inquiries delve into the fundamental nature of matter and the Universe, aiming to unravel the intricate behavior of quarks and gluons that make up

[*]liuxinyi23@mails.ucas.ac.cn
[†]pengxc1616@mails.jlu.edu.cn
[‡]ylwu@itp.ac.cn
[§]zhenfang@hnu.edu.cn

protons, neutrons, and other hadrons. Understanding the QCD phase transition, which occurs under extreme conditions of temperature and baryon chemical potential, such as those in the early Universe or within neutron stars, is critical for our comprehension of the fundamental forces governing the cosmos [1]. The QCD phase diagram, on the other hand, provides a comprehensive map of the different phases of nuclear matter and offers essential insights into the behavior of matter at various temperatures and densities. These investigations not only deepen our understanding of the building blocks of matter but also have practical applications, ranging from high-energy physics to astrophysics, impacting the way we perceive the Universe and its evolution.

One of the key issues is to study the nature of QCD phase transition that takes place in hot and dense environments. QCD is known to exhibit two distinct types of phase transitions in these extreme conditions, namely the chiral

and the deconfinement phase transitions. At low temperature T and small baryon chemical potential μ_B, QCD matter predominantly exists as confined hadrons due to strong quark confinement, with a nonzero chiral condensate that contributes to the hadron mass. As temperature rises, QCD matter will finally enter a deconfined phase of quark-gluon plasma through a smooth crossover, with the chiral condensate approaching zero and the chiral symmetry restored [1–3]. It is commonly believed that the phase transition between hadronic matter and quark-gluon plasma changes from a smooth crossover to a first-order phase transition with the increase of μ_B. Hence, the existence and properties of the critical end point (CEP) of the first-order transition line are essential for understanding the behavior of QCD matter under extreme conditions. The location of CEP depends on factors like the number of quark flavors and the strength of interactions. In extremely dense conditions, such as in the core of neutron stars, quark matter may undergo color superconductivity and exhibits novel phases [4].

Efforts to understand the QCD phase transition and to construct the QCD phase diagram have been a focal point of both theoretical and experimental researches in the field of nuclear and particle physics. In the Large Hadron Collider at CERN and the Relativistic Heavy Ion Collider at Brookhaven National Laboratory, high-energy nuclear collisions have been conducted to recreate conditions similar to the early Universe, allowing us to investigate the properties of QCD matter under extreme conditions. Neutron star astrophysics and gravitational wave observations also offer indirect insights into the behavior of dense nuclear matter under extreme conditions. Theoretical attempts at studying the QCD phase transition involve lattice QCD simulations [5,6] and model calculations, such as the chiral effective model and various other theoretical frameworks [7–12]. However, almost all the methods come with shortages and difficulties related to the nonperturbative nature of low-energy QCD. For the lattice QCD, the infamous sign problem exists when addressing issues at finite baryon density, even though various systematic schemes have been constructed to extrapolate the lattice results to finite baryon chemical potentials [13–15].

In the last two decades, the gauge/gravity duality, also known as the AdS/CFT correspondence [16–18], has been established as a promising approach to solve various strong-coupling related problems, especially the nonperturbative aspects of QCD [19–21]. Indeed, it has been a long desire to construct a holographic dual of QCD, which is called the anti–de Sitter (AdS)/QCD program, aiming to provide quantitative descriptions for the low-energy QCD properties that is intrinsically nonperturbative. This includes the study of the hadron spectrum, the thermodynamic properties and also the phase structure of QCD. Many holographic QCD models have been constructed by a bottom-up approach, in consideration of the basic features of low-energy QCD, such as the spontaneous chiral symmetry breaking and the linear confinement property [22–66]. The well-known ones include the hard-wall and soft-wall models [23–25], the modified versions of which could produce the light hadron spectra in agreement with measurements, and could also realize the proper chiral transition behaviors in the case of both two and $2 + 1$ flavors [67–75]. The equation of state and the associated deconfinement phase transition at $\mu_B = 0$ have been studied in the holographic framework by an Einstein-dilaton system with a suitable dilaton potential [76–93], while the Einstein-Maxwell-dilaton (EMD) system has been used to investigate the properties of QCD phase transition at $\mu_B \neq 0$ and to construct the QCD phase diagram [94–96]. However, the chiral and deconfinement phase transitions, as two sides of one coin, should be realized simultaneously in a consistent way. For that, some efforts have been made to characterize these two kinds of phase transitions in a single holographic framework [97–102].

In this work, we attempt to construct a holographic QCD model with the aim to provide a proper description for both the equation of state and the chiral transition at finite μ_B in the two-flavor case. The matter part of this model will be given by an improved soft-wall model that could generate spontaneous chiral symmetry breaking and realize the right chiral transition properties, at least qualitatively. The bulk background will be given by an EMD system which could describe the equation of state and the expected deconfinement properties of QCD. By integrating these two sectors into an Einstein-Maxwell-dilaton-scalar (EMDS) system, we find that the properties of deconfinement and chiral transitions could be characterized consistently in this holographic framework. Furthermore, we find that the model results of the equation of state at finite μ_B are in good agreement with the lattice results of two flavors, and the QCD phase diagram containing a CEP can also be obtained. After fixing the model parameters, we also investigate the equation of state in the reduced EMD system with the coupling $\beta = 0$, and we find that the phase transition is a first-order one at $\mu_B = 0$, which is consistent with that of the pure gauge sector of QCD [103,104]. This feature is very different from that given in the previous work [101], where we only gave a qualitative investigation on the phase transition in a simple Einstein-dilaton-scalar system at zero chemical potential.

The paper is organized as follows. In Sec. II, we outline the holographic QCD model, and then focus on the EMDS system that will be mainly addressed. The equation of motion will be derived from the action of the model, and the boundary condition will be given for numerical calculation. In Sec. III, we investigate the QCD phase transition at finite μ_B in the EMDS system and show the numerical results. The model parameters will be fixed by fitting the two-flavor lattice results of the equation of state at $\mu_B = 0$. We then obtain the equation of state and the chiral transition at

finite μ_B. The QCD phase diagram will also be obtained from the model. In Sec. IV, we give a conclusion on our work with a few discussions.

II. THE IMPROVED SOFT-WALL AdS/QCD MODEL COUPLED WITH AN EMD SYSTEM

The action of the two-flavor holographic QCD model can be divided into two parts: $S = S_G + S_M$. The part of gravitational background is an EMD system that can be written in the string frame,

$$S_G = \frac{1}{2\kappa_5^2} \int d^5x \sqrt{-g} e^{-2\phi} [R - h(\phi)F_{MN}F^{MN} + 4(\partial\phi)^2 - V(\phi)], \quad (1)$$

where $\kappa_5^2 = 8\pi G_5$ is the effective Newton constant. The chemical potential effects can be introduced into the system by the Abelian gauge field A_M of the action. The dilaton ϕ has been included to break the conformal symmetry, in order to give a sensible description for QCD phase transition [76]. Later we will specify the form of the dilaton potential $V(\phi)$ and also the gauge kinetic function $h(\phi)$ that characterizes the coupling strength of the gauge field A_M.

The flavor part of the action comes from an improved soft-wall AdS/QCD model with an additional coupling term of the Abelian gauge field and the bulk scalar field:

$$S_M = -\kappa \int d^5x \sqrt{-g} e^{-\phi} \mathrm{Tr} \Big\{ |DX|^2 + V_X(X, \phi) + \tilde{\lambda}_3(\phi)F_{MN}F^{MN}|X|^2 + \frac{1}{4g_5^2}(F_L^2 + F_R^2) \Big\}, \quad (2)$$

where the covariant derivative $D^M X = \partial^M X - iA_L^M X + iXA_R^M$, and the chiral gauge field strength takes the form $F_{L,R}^{MN} = \partial^M A_{L,R}^N - \partial^N A_{L,R}^M - i[A_{L,R}^M, A_{L,R}^N]$. The coupling term $\tilde{\lambda}_3(\phi)$ will be fixed below. The potential for the bulk scalar and the dilaton takes the form

$$V_X(X, \phi) = m_5^2|X|^2 - \lambda_1\phi|X|^2 + \lambda_2|X|^4, \quad (3)$$

where the bulk scalar mass is determined by the mass-dimension relation $m_5^2 L^2 = \Delta_X(\Delta_X - 4)$ with $\Delta_X = 3$ being the scaling dimension of the dual operator $\bar{q}_R q_L$ of the scalar field in the boundary [24].

The potential V_X in Eq. (3) has been applied to investigate thermodynamic properties of QCD in the case of $\mu_B = 0$ [100,101], which shows that such a form of V_X could provide a good description for both the equation of state and the chiral transition, at least on the qualitative level. Thus it seems natural for us to generalize to the finite chemical potential case in order to check whether this type of holographic QCD model could still produce consistent

results of QCD phase transition with other models or lattice simulations. The coupling term of the Abelian gauge field and the bulk scalar field in Eq. (2) has also been considered in previous studies with the aim to realize the correct behaviors of chiral transition at finite μ_B [105]. We remark that the role of this coupling term is in some sense like that in Ref. [105] but in a rather different model setup.

The holographic QCD model is built in a gravitational background with the metric ansatz

$$ds^2 = \frac{L^2 e^{2A_S(z)}}{z^2} \Big(-f(z)dt^2 + dx^i dx^i + \frac{dz^2}{f(z)} \Big), \quad (4)$$

where L is the curvature radius of the asymptotic AdS$_5$ spacetime. Without loss of generality, we just take $L = 1$ below. At finite temperature, this metric represents an asymptotic AdS black hole to be solved from the equation of motion of the system. We require $f(z_h) = 0$ at the event horizon z_h of the black hole.

A. The Einstein-Maxwell-dilaton-scalar system

According to Ref. [24], the vacuum expectation value (VEV) of the bulk scalar field X can be written as $\langle X \rangle = \frac{\chi(z)}{2} I_2$ with I_2 denoting the 2×2 unit matrix, and the chiral condensate σ is embodied in the UV expansion of the scalar VEV $\langle X \rangle$. In order to investigate the properties of chiral transition, we only need to consider the vacuum part of matter fields represented by $\langle X \rangle$ in the bulk action (2) and neglect the vacuum fluctuations corresponding to the meson fields. Thus the holographic QCD model is reduced to an EMDS system:

$$S = S_G + S_\chi,$$
$$= \frac{1}{2\kappa_5^2} \int d^5x \sqrt{-g} e^{-2\phi} \Big[R - h(\phi)F_{MN}F^{MN} + 4(\partial\phi)^2$$
$$- V(\phi) - \beta e^\phi \Big(\frac{1}{2}(\partial\chi)^2 + V(\chi, \phi)$$
$$+ \frac{\tilde{\lambda}_3(\phi)}{2}F_{MN}F^{MN}\chi^2 \Big) \Big], \quad (5)$$

where $\beta = 16\pi G_5 \kappa$ controls the coupling strength between the bulk background and the matter part, and the potential for the scalar VEV χ and the dilaton ϕ takes the form

$$V(\chi, \phi) = \mathrm{Tr} V_X(\langle X \rangle, \phi),$$
$$= \frac{1}{2}(m_5^2 - \lambda_1\phi)\chi^2 + \frac{\lambda_2}{8}\chi^4. \quad (6)$$

For convenience, we usually transform to the Einstein frame by taking the metric ansatz

$$ds^2 = \frac{L^2 e^{2A_E(z)}}{z^2}\left(-f(z)dt^2 + dx^i dx^i + \frac{dz^2}{f(z)}\right) \quad (7)$$

with the warp factor $A_E(z)$ related to the string-frame factor $A_S(z)$ by $A_E = A_S - \frac{2}{3}\phi$. The bulk action (5) in the Einstein frame can then be written as

$$S = \frac{1}{2\kappa_5^2}\int d^5x\sqrt{-g_E}\left[R_E - \omega(\phi)F_{MN}F^{MN}\right.$$
$$-\frac{4}{3}(\partial\phi)^2 - V_E(\phi) - \beta e^\phi\left(\frac{1}{2}(\partial\chi)^2 + V_E(\chi,\phi)\right)$$
$$\left.+\frac{\hat{\lambda}_3(\phi)}{2}F_{MN}F^{MN}\chi^2\right)\right], \quad (8)$$

where

$$\omega(\phi) = h(\phi)e^{\frac{4\phi}{3}},$$
$$V_E(\phi) = e^{\frac{4\phi}{3}}V(\phi),$$
$$V_E(\chi,\phi) = e^{\frac{4\phi}{3}}V(\chi,\phi),$$
$$\hat{\lambda}_3(\phi) = \tilde{\lambda}_3(\phi)e^{-\frac{4}{3}\phi}. \quad (9)$$

We could do a rescaling $\phi_c = \sqrt{8/3}\phi$ to convert the kinetic term of the dilaton ϕ to a canonical one. Following Ref. [76], we adopt a simpler form of the dilaton potential

$$V_c(\phi_c) = \frac{1}{L^2}(-12\cosh\gamma\phi_c + b_2\phi_c^2 + b_4\phi_c^4), \quad (10)$$

and take $V_E(\phi) = V_c(\phi_c)$. This guarantees the bulk geometry to have an asymptotic AdS structure near the boundary:

$$V_c(\phi_c \to 0) \simeq \frac{-12}{L^2} + \frac{b_2 - 6\gamma^2}{L^2}\phi_c^2 + \mathcal{O}(\phi_c^4). \quad (11)$$

The mass-dimension relation gives

$$b_2 = 6\gamma^2 + \frac{\Delta(\Delta-4)}{2}, \quad (12)$$

where Δ denotes the scaling dimension of the dual operator of the dilaton field. As shown in Ref. [101], the specific value of Δ in the Breitenlohner-Freedman bound actually does not affect the qualitative behaviors of phase transition. Thus we just take $\Delta = 3$ for simplicity.

We adopt a form of the gauge kinetic function

$$\omega(\phi) = \frac{c_0}{4}e^{-c_1\phi_c} + \frac{1-c_0}{4\,\mathrm{sech}(c_3 c_4)}\mathrm{sech}[c_3(\phi_c - c_4)], \quad (13)$$

which approaches $1/4$ as $\phi_c \to 0$ in the UV limit. Such a form of $\omega(\phi)$ is inspired by those considered in Refs. [94,95], which provide a suitable description for

the quark susceptibility at $\mu_B = 0$. For the last unfixed function $\hat{\lambda}_3(\phi)$, we will adopt a simple exponential form $\hat{\lambda}_3(\phi) = \lambda_3 e^{k\phi}$ in order to produce proper chiral transition behaviors at finite μ_B. We remark that the coupling term related to $\hat{\lambda}_3$ has few influences on the equation of state at finite μ_B.

B. Equation of motion and boundary condition

By the variational method, the Einstein field equation and the equations of motion for the Abelian gauge field A_M, the dilaton ϕ, and the scalar VEV χ can be derived from the action (8) as

$$R_{MN} - \frac{1}{2}g_{MN}R + \omega(\phi)\left(\frac{1}{2}g_{MN}F_{AB}F^{AB} - 2F_{MA}F_N{}^A\right)$$
$$+\frac{4}{3}\left(\frac{1}{2}g_{MN}\partial_J\phi\partial^J\phi - \partial_M\phi\partial_N\phi\right) + \frac{1}{2}g_{MN}V_E(\phi)$$
$$+\frac{\beta}{2}e^\phi\left(\frac{1}{2}g_{MN}\partial_J\chi\partial^J\chi - \partial_M\chi\partial_N\chi\right) + \frac{\beta}{2}g_{MN}e^\phi V_E(\chi,\phi)$$
$$+\frac{\beta}{2}\hat{\lambda}_3(\phi)e^\phi\left(\frac{1}{2}F_{AB}F^{AB}g_{MN} - 2F_{MA}F_N{}^A\right)\chi^2 = 0, \quad (14)$$

$$\nabla_M\left[w(\phi)F^{MN} + \frac{\beta}{2}\hat{\lambda}_3(\phi)e^\phi\chi^2 F^{MN}\right] = 0, \quad (15)$$

$$\frac{8}{3}\nabla_M\nabla^M\phi - \partial_\phi w(\phi)F_{MN}F^{MN} - \partial_\phi V_E(\phi)$$
$$-\frac{\beta}{2}e^\phi g^{MN}\partial_M\chi\partial_N\chi - \beta\partial_\phi[e^\phi V_E(\chi,\phi)]$$
$$-\frac{\beta}{2}\partial_\phi[\hat{\lambda}_3(\phi)e^\phi]F_{MN}F^{MN}\chi^2 = 0, \quad (16)$$

$$\nabla_M(e^\phi\nabla^M\chi) - \hat{\lambda}_3(\phi)e^\phi F_{MN}F^{MN}\chi$$
$$- e^\phi\partial_\chi V_E(\chi,\phi) = 0. \quad (17)$$

At finite chemical potential, we only keep the time-component A_t of the Abelian gauge field to be nonzero. In terms of the metric ansatz (7) and the assumption that the bulk fields depend only on the fifth-dimension coordinate z, Eqs. (14)–(17) can then be simplified to the following five independent equations:

$$f'' + 3A_E'f' - \frac{3}{z}f' - 4z^2\omega(\phi)e^{-2A_E}A_t'^2$$
$$- 2\beta z^2\hat{\lambda}_3(\phi)e^{-2A_E+\phi}\chi^2 A_t'^2 = 0, \quad (18)$$

$$A_E'' + \frac{2}{z}A_E' - A_E'^2 + \frac{4}{9}\phi'^2 + \frac{\beta}{6}e^\phi\chi'^2 = 0, \quad (19)$$

$$A_t'' + \frac{A_t'}{2ze^{\phi}\omega(\phi) + \beta z\hat{\lambda}_3(\phi)e^{2\phi}\chi^2}[2\omega(\phi)e^{\phi}(zA_E' - 1)$$
$$+ 2ze^{\phi}\partial_{\phi}\omega(\phi)\phi' + \beta ze^{2\phi}\partial_{\phi}\hat{\lambda}_3(\phi)\phi'\chi^2$$
$$+ \beta\hat{\lambda}_3(\phi)e^{2\phi}(\chi^2(zA_E' + z\phi' - 1) + 2z\chi\chi')] = 0, \quad (20)$$

$$\phi'' + \left(3A_E' + \frac{f'}{f} - \frac{3}{z}\right)\phi' - \frac{3\beta}{16}e^{\phi}\chi'^2 - \frac{3e^{2A_E}\partial_{\phi}V_E(\phi)}{8z^2f}$$
$$+ \frac{3z^2e^{-2A_E}A_t'^2\partial_{\phi}\omega(\phi)}{4f} - \frac{3\beta e^{2A_E}\partial_{\phi}(e^{\phi}V_E(\chi,\phi))}{8z^2f}$$
$$+ \frac{3\beta z^2e^{\phi-2A_E}\chi^2A_t'^2}{8f}(\hat{\lambda}_3(\phi) + \partial_{\phi}\hat{\lambda}_3(\phi)) = 0, \quad (21)$$

$$\chi'' + \left(3A_E' + \phi' + \frac{f'}{f} - \frac{3}{z}\right)\chi' - \frac{e^{2A_E}\partial_{\chi}V_E(\chi,\phi)}{z^2f}$$
$$+ \frac{2z^2\hat{\lambda}_3(\phi)e^{-2A_E}}{f}A_t'^2\chi = 0, \quad (22)$$

where the function $f(z)$ and the electrostatic potential $A_t(z)$ are required to satisfy the following boundary conditions:

$$f(0) = 1, \qquad f(z_h) = 0, \qquad (23)$$

$$A_t(0) = \mu_B, \qquad A_t(z_h) = 0. \qquad (24)$$

The UV asymptotic solution for Eqs. (18)–(22) can be obtained as

$$f(z) = 1 - f_4z^4 + \cdots, \qquad (25)$$

$$A_E(z) = -\frac{1}{108}(3\beta m_q^2\zeta^2 + 8p_1^2)z^2$$
$$- \frac{1}{24}\beta p_1 m_q^2\zeta^2(2\lambda_1 + 11)z^3 + \cdots, \quad (26)$$

$$A_t(z) = \mu_B - \kappa_5^2 n_B z^2 - \frac{4\sqrt{6}}{9}p_1\kappa_5^2 n_B[c_0c_1$$
$$+ (c_0 - 1)c_3\tanh(c_3c_4)]z^3 + \cdots, \quad (27)$$

$$\phi(z) = p_1 z + \frac{3}{16}\beta m_q^2\zeta^2(\lambda_1 + 6)z^2 + p_3z^3$$
$$- \left[\frac{1}{48}\beta p_1 m_q^2\zeta^2(9\lambda_1^2 + 111\lambda_1 + 286)\right.$$
$$\left. - \frac{4}{9}p_1^3(12b_4 - 6\gamma^4 + 1)\right]z^3\ln z + \cdots, \quad (28)$$

$$\chi(z) = m_q\zeta z + p_1 m_q\zeta(\lambda_1 + 5)z^2 + \frac{\sigma}{\zeta}z^3$$
$$- \left[\frac{1}{96}m_q^3\zeta^3(\beta(9\lambda_1^2 + 108\lambda_1 + 308) - 24\lambda_2)\right.$$
$$\left. + \frac{1}{18}p_1^2 m_q\zeta(9\lambda_1^2 + 111\lambda_1 + 286)\right]z^3\ln z + \cdots, \quad (29)$$

where $\zeta = \frac{\sqrt{3}}{2\pi}$ is a normalization constant [27], m_q denotes the current quark mass, σ the chiral condensate, and n_B the baryon number density. From the UV expansions (25)–(29), we read another two conditions:

$$\phi'(0) = p_1, \qquad \chi'(0) = m_q\zeta. \qquad (30)$$

In terms of the boundary conditions (23), (24), and (30), the bulk fields can be solved numerically from Eqs. (18)–(22) (see the Appendix). The baryon number density n_B and the chiral condensate σ can then be extracted from the UV asymptotics of A_t and χ, respectively.

III. QCD PHASE TRANSITION AT FINITE CHEMICAL POTENTIAL

A. Equation of state and chiral transition

Once we could solve the EMDS system, the equations of state and the chiral transition can be investigated simultaneously at finite μ_B. The temperature and the entropy density are given by the formulas:

$$T = \frac{|f'(z_h)|}{4\pi}, \qquad s = \frac{2\pi e^{3A_E(z_h)}}{\kappa_5^2 z_h^3}. \qquad (31)$$

The pressure p can be calculated by the differential relation

$$dp = sdT + n_q d\mu_q, \qquad (32)$$

and the energy density can then be obtained from the thermodynamic relation $\varepsilon = -p + sT + \mu_q n_q$, with the quark number density $n_q = 3n_B$ and the quark chemical potential $\mu_q = \mu_B/3$.

To do the numerical calculation, we need to fix the model parameters, which could be determined by fitting the lattice results of the equation of state in the two-flavor case [106,107]. First note that we can always set the background-matter coupling to be $\beta = 1$ by rescaling the scalar VEV χ and other parameters in our model. The current quark mass will be taken as $m_q = 5$ MeV. By fitting the equation of state at $\mu_q = 0$, we can fix the parameters $G_5 = 0.582$, $\gamma = 0.75$, $b_4 = 0.02$, and $p_1 = 0.473$ GeV. Other parameters of the model are related to the chemical potential effects and the properties of chiral transition. For instance, the values of the coefficients c_0, c_1, c_3, c_4, and λ_3, k have direct effects on the equation of state at finite μ_q. In order to fix these parameters, we could use the quark susceptibility defined by

$$\chi_2^q = \frac{\partial^2(P/T^4)}{\partial(\mu_q/T)^2} = \frac{\partial(n_q/T^3)}{\partial(\mu_q/T)}. \qquad (33)$$

The values of λ_1, λ_2, λ_3, and k are crucial for a proper realization of the chiral transition behaviors at finite μ_q.
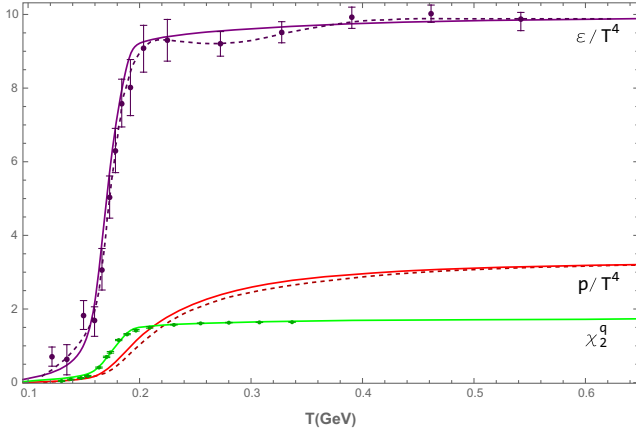
FIG. 1. Comparison of the model results for the scaled energy density ϵ/T^4, the pressure p/T^4, and the quark susceptibility χ_2^q with the lattice results at $\mu_q = 0$. The model results are denoted by solid lines, while the lattice data are denoted by dashed lines or points with error bars [106,107].

Since the background fields and the matter fields are coupled with each other, the thermodynamic properties at finite μ_q actually depend on all the parameters of the model. By a global fitting, we can fix the remaining parameters to be $c_0 = 0.725$, $c_1 = 30$, $c_3 = 0.47$, $c_4 = 0.45$, $\lambda_1 = -1$, $\lambda_2 = 10$, $\lambda_3 = -0.65$, and $k = -1.67$.

In Fig. 1, we present the model calculations for the scaled energy density ϵ/T^4, the pressure p/T^4 and the quark susceptibility χ_q/T^2 at $\mu_q = 0$, which have been used to fix the parameters of the model. We can see that the model results have a good match with the lattice results in the two-flavor case [106,107]. Then we can apply our model to investigate the properties of the equation of state and the chiral transition at nonzero chemical potential. In Fig. 2, we present the model results for the scaled pressure $\Delta p/T^4$ with $\Delta p = p(T, \mu_q) - p(T, 0)$ and the quark number density n_q/T^3 at fixed values of μ_q/T, which are compared with the lattice results in the two-flavor case. We find that the model results are in good agreement with the lattice data.

We also investigate the behaviors of the equation of state and the chiral transition with fixed values of μ_q. We present the temperature T as a function of the horizon z_h at five different values of μ_q in Fig. 3, from which we find that for smaller values of μ_q, the temperature decreases monotonically with the event horizon. However, when μ_q increases beyond a critical point $\mu_q^E \simeq 423$ MeV, the behavior of T with respect to z_h will become nonmonotonic in a small region of z_h, which signals that the transition order of the thermodynamic quantities obtained from the model will be changed around the critical value μ_q^E. The chiral transition behaviors with fixed μ_q are presented in Fig. 4, from which we can see that the chiral transition is a smooth crossover at smaller values of μ_q, yet when μ_q becomes larger and
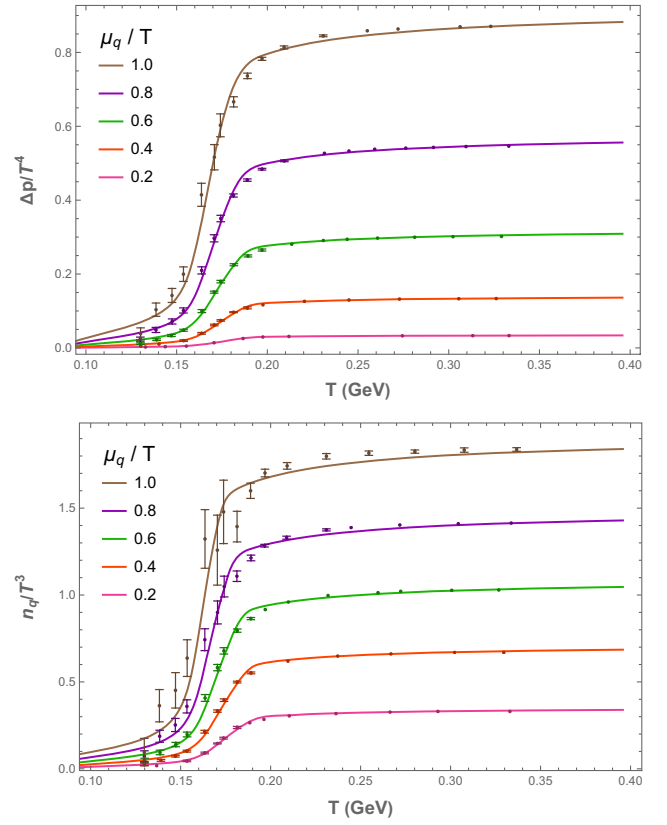

FIG. 2. Comparison of the model results for the scaled pressure $\Delta p/T^4$ and the quark number density n_q/T^3 with the lattice results for $\mu_q/T = 0.2, 0.4, 0.6, 0.8, 1$. The lattice data are taken from Refs. [106,108].
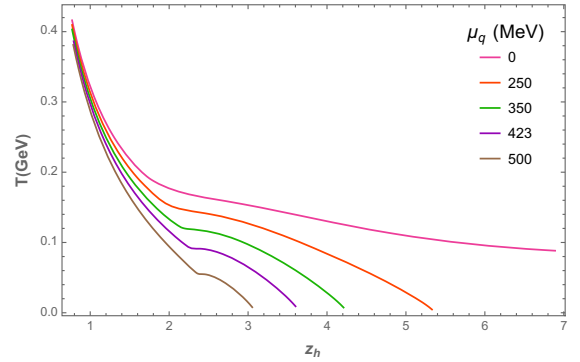

FIG. 3. The temperature T as a function of the horizon z_h at $\mu_q = 0, 250, 350, 423, 500$ MeV.

larger, the chiral condensate σ descends more and more rapidly with the increase of temperature T in the transition region, until μ_q reaches the critical point μ_q^E, at which the chiral transition becomes a second-order phase transition, and then it converts to a first-order phase transition when μ_q is larger than μ_q^E. These behaviors of chiral transition with respect to the chemical potential are consistent with that of the $T - z_h$ curves in Fig. 3.
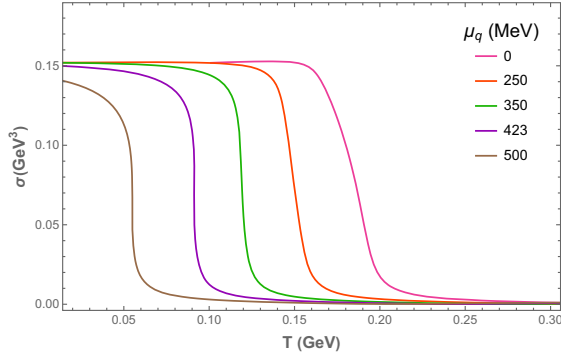
FIG. 4.   The behaviors of the chiral condensate σ with respect to the temperature T at $\mu_q = 0, 250, 350, 423, 500$ MeV.

Note that the change of the transition order is not that obvious from the chiral transition behaviors shown in Fig. 4. We then calculate the scaled entropy density s/T^3 and the free energy $F = -p$ around the critical point μ_q^E. In Fig. 5, we present the model results for three neighboring values of μ_q, from which we can see clearly that the free-energy line displays a swallow-tail shape at $\mu_q = 443$ MeV, which is a clear signal for a first-order phase transition. The intersection point of the free-energy line determines the critical temperature of the first-order transition.
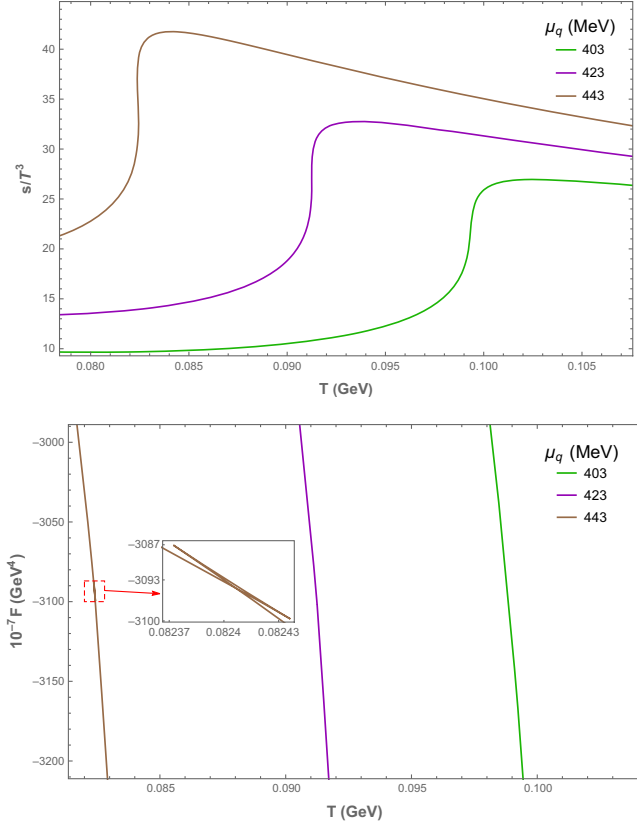

FIG. 5.   The behaviors of the scaled entropy density s/T^3 and the free energy F around the transition temperature for $\mu_q = 403, 423, 443$ MeV.

B. QCD phase diagram

We can obtain the QCD phase diagram as long as we could determine the transition temperature at each chemical potential, which can be attained from the analysis of the equation of state and the chiral transition. As mentioned above, the critical temperature T_c for the first-order phase transition at large μ_q can be determined by the intersection point of the free-energy line. As μ_q decreases to $\mu_q^E \simeq 423$ MeV, the swallow-tail shape of the free-energy line disappears, with the critical temperature $T^E \simeq 91.2$ MeV, at which a second-order phase transition occurs. The phase transition turns into a smooth crossover below μ_q^E. There is no unique way to determine the transition temperature T_c for the crossover case. We may use the minimum of the speed of sound c_s, which is a suitable probe to characterize the drastic change of degrees of freedom between the confinement phase of hadrons and the deconfinement phase of quark-gluon plasma. In addition, we may also use the maximally decreasing point of the chiral condensate σ to signify the chiral transition temperature.

The model prediction for the QCD phase diagram is presented in Fig. 6, where we use the baryon chemical potential μ_B, instead of the quark chemical potential μ_q. Note that there is a CEP located at $(\mu_B^E, T^E) = (1268 \text{ MeV}, 91.2 \text{ MeV})$, which links the first-order transition line in the range of $\mu_B > \mu_B^E$ with the crossover transition line in the range of $\mu_B < \mu_B^E$. It seems that the critical point μ_B^E of our model with two flavors is larger than those obtained from other models including a recent holographic study on the phase structure of two-flavor QCD [109–113]. It can be seen from Fig. 6 that the two crossover lines given by the minimum of c_s and the σ inflection do not coincide, with the chiral transition temperature greater than the deconfinement transition temperature at smaller values of μ_B, and they converge gradually to the CEP with the increase of μ_B. At $\mu_B = 0$, the transition
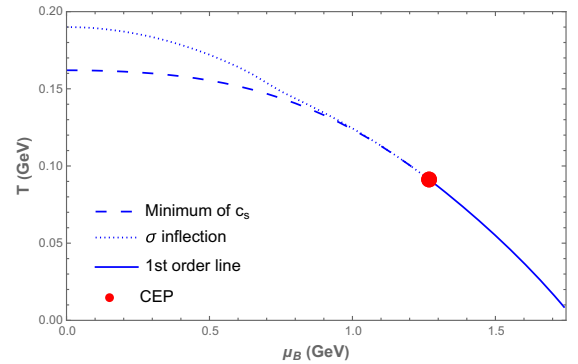

FIG. 6.   The QCD phase diagram obtained from the model. The minimum of the speed of sound c_s and the maximally decreasing point of the chiral condensate σ are denoted by the dashed and dotted lines, respectively. The first-order transition is denoted by a solid line. The CEP is marked by a red point.

temperature determined by the minimum of c_s is about 162 MeV, while the chiral transition temperature is about 190 MeV.

C. Pure gauge sector

With suitable choice of parameters, the EMDS system with the action (5) is capable of describing both the equation of state and the chiral transition at finite chemical potential, and the properties of phase transition obtained from the model are consistent with the lattice results and the common expectations. Now we would like to decouple the matter part with the bulk background by setting $\beta = 0$. It is interesting to see how the equation of state and other thermodynamic quantities behave in the reduced EMD system which may holographically characterize the gluon dynamics of QCD.

We calculate the scaled entropy density s/T^3, the energy density ϵ/T^4, and the pressure p/T^4 at zero chemical potential in this EMD system with the fixed parameters. The numerical results are presented in Fig. 7. Clearly, the EMD system of this model exhibits a first-order phase transition at $\mu_q = 0$, which is qualitatively consistent with the lattice simulations for pure Yang-Mills theory [103,104]. The free-energy line in this case has been shown
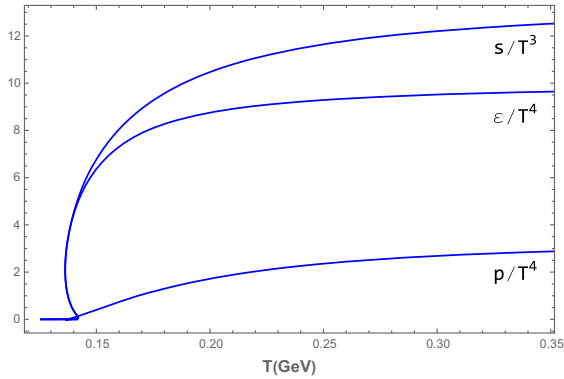

FIG. 7. The scaled entropy density s/T^3, the energy density ϵ/T^4, and the pressure p/T^4 at $\mu_q = 0$ in the case of $\beta = 0$.
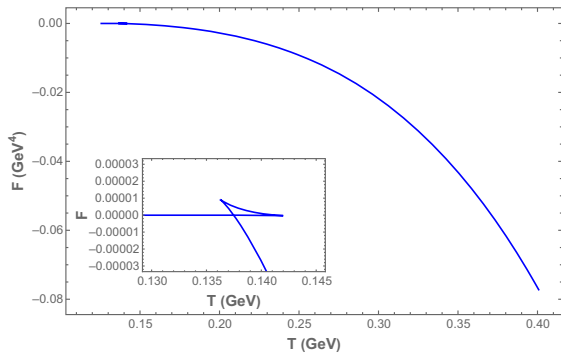

FIG. 8. The free energy F at $\mu_q = 0$ in the case of $\beta = 0$.

in Fig. 8, from which we can read the critical temperature $T_c \simeq 137.5$ MeV.

IV. CONCLUSION AND DISCUSSION

We investigated the properties of phase transition and phase diagram in an improved soft-wall AdS/QCD model coupled with an EMD system in the two-flavor case. With fixed parameters, this model yields the equation of state in quantitative agreement with the lattice results of two flavors at both zero and nonzero chemical potentials. It also generates sensible chiral transition behaviors consistent with the equation of state at finite chemical potential. Note that the deconfinement and chiral transitions are interrelated with each other, and occur simultaneously in the first-order transition region of large μ_B. This is a natural result of the fact that the bulk background fields and the vacuum scalar field have been coupled together. But in the crossover region, because of different order parameters being used, the transition temperatures obtained from them are also different. In addition, we find that the first-order phase transition beyond μ_B^E is actually very weak in our model, as can be seen by the free-energy lines in Fig. 5.

The QCD phase diagram in the $T - \mu_B$ plane has been obtained, with a CEP located at $(\mu_B^E, T^E) = (1268$ MeV, 91.2 MeV$)$. The large value of the critical point μ_B^E in our model forms an obvious contrast to those obtained from the previous studies [109–112]. By the equation of state, we also find that the reduced EMD system of our model generates a first-order phase transition at zero chemical potential, which is consistent with that of the pure gauge theory [103,104]. To sum up, all these features indicate that the phase structure of our model is quite similar to that of QCD, at least on a qualitative level, as long as μ_B is not too large. We may wonder whether a more quantitative description for the phase structure of QCD could be obtained from such a holographic framework.

For a convincing description of the QCD phase transition, we actually need to give the information of hadron spectrum. It remains to be seen whether the mass spectra of light hadrons could be reproduced in this holographic QCD model. It will be interesting to generalize the two-flavor investigations of this work to the $2 + 1$ flavor case by introducing another vacuum scalar field related to the strange flavor, in which case we may have other ways to obtain the QCD phase diagram containing a CEP. With the rise of the astronomy of neutron stars and gravitational waves, it will also be interesting to apply this holographic QCD model to investigate the equation of state and other properties of neutron stars.

APPENDIX: IMPLEMENTATION OF SPECTRAL COLLOCATION METHOD IN OUR MODEL

We now detail the implementation of the spectral collocation method for the numerical calculation. First we change the form of Eqs. (18)–(22) by applying the following two transformations successively:

$$z \to uz_h, \quad f(z) \to \hat{f}(u), \quad A_E(z) \to \hat{A}_E(u)$$
$$A_t(z) \to \hat{A}_t(u), \quad \phi(z) \to \hat{\phi}(u), \quad \chi(z) \to \hat{\chi}(u); \quad \text{(A1)}$$

$$u \to \frac{t+1}{2}, \qquad\qquad \hat{f}(u) \to \tilde{f}(t),$$
$$\hat{A}_E(u) \to \left(\frac{t+1}{2}\right)^2 \tilde{A}_E(t), \quad \hat{A}_t(u) \to \tilde{A}_t(t),$$
$$\hat{\phi}(u) \to \frac{t+1}{2}\tilde{\phi}(t), \qquad \hat{\chi}(u) \to \frac{t+1}{2}\tilde{\chi}(t). \quad \text{(A2)}$$

Equations (18)–(22) are then transformed into the desired form with t as the independent variable. Since the final expressions are too lengthy to be presented here, we just show the changed form of Eq. (19),

$$a_1(t)\tilde{A}_E''(t) + a_2(t)\tilde{A}_E'(t) + a_3(t)\tilde{A}_E(t)\tilde{A}_E'(t)$$
$$+ a_4(t)\tilde{A}_E'(t)^2 + a_5(t)\tilde{A}_E(t)$$
$$+ a_6(t)\tilde{A}_E(t)^2 + a_7(t) = 0, \qquad\qquad \text{(A3)}$$

where $t \in (-1, 1)$ and the coefficient functions are

$$a_1(t) = 36(t+1)^2, \qquad\qquad \text{(A4)}$$

$$a_2(t) = 216(t+1), \qquad\qquad \text{(A5)}$$

$$a_3(t) = -36(t+1)^3, \qquad\qquad \text{(A6)}$$

$$a_4(t) = -9(t+1)^4, \qquad\qquad \text{(A7)}$$

$$a_5(t) = 216, \qquad\qquad \text{(A8)}$$

$$a_6(t) = -36(t+1)^2, \qquad\qquad \text{(A9)}$$

$$a_7(t) = 2\{8\tilde{\phi}(t)^2 + 3e^{\frac{1}{2}(t+1)\tilde{\phi}(t)}\beta\tilde{\chi}(t)^2$$
$$+16(t+1)\tilde{\phi}(t)\tilde{\phi}'(t) + 6e^{\frac{1}{2}(t+1)\tilde{\phi}(t)}(t+1)\beta\tilde{\chi}(t)\tilde{\chi}'(t)$$
$$+(t+1)^2[8\tilde{\phi}'(t)^2 + 3e^{\frac{1}{2}(t+1)\tilde{\phi}(t)}\beta\tilde{\chi}'(t)^2]\}. \quad \text{(A10)}$$

The boundary conditions (23), (24), and (30) now become

$$\tilde{f}(-1) = 1, \qquad\qquad \text{(A11)}$$

$$\tilde{f}(1) = 0, \qquad\qquad \text{(A12)}$$

$$\tilde{A}_t(-1) = \mu_B, \qquad\qquad \text{(A13)}$$

$$\tilde{A}_t(1) = 0, \qquad\qquad \text{(A14)}$$

$$\tilde{\phi}(-1) = p_1 z_h, \qquad\qquad \text{(A15)}$$

$$\tilde{\chi}(-1) = \zeta m_q z_h. \qquad\qquad \text{(A16)}$$

Next, let us first select a set of distinct collocation points $\{t_i\}_{i=0}^N$ ($N \geq 1$ is an integer) on $[-1, 1]$ with $\{t_i\}_{i=0}^N$ being the $N+1$ roots of the equation

$$(1 - t^2)\frac{d}{dt}L_N(t) = 0, \qquad\qquad \text{(A17)}$$

where $L_N(t)$ is the Nth Legendre polynomial. The derivative matrix $\mathbf{D}$ is an $(N+1) \times (N+1)$ matrix, which is given by

$$\mathbf{D}_{ij} = \begin{cases} -\frac{N(N+1)}{4}, & i = j = 0 \\ 0, & 1 \leq i = j \leq N-1 \\ \frac{N(N+1)}{4}, & i = j = N \\ \frac{L_N(x_i)}{(x_i - x_j)L_N(x_j)}, & i \neq j \end{cases} . \quad \text{(A18)}$$

Note that the range of each index of the matrix $\mathbf{D}$ is $[0, N]$. For a general function $f(t)$, $f(t_i)$ denotes the value of $f(t)$ at the collocation point t_i. The value of the derivative function $f'(t)$ can be calculated by the differential matrix

$$\overrightarrow{\mathbf{f'(t)}} = \mathbf{D}\overrightarrow{\mathbf{f(t)}}, \qquad\qquad \text{(A19)}$$

where

$$\overrightarrow{\mathbf{f(t)}} = \begin{pmatrix} f(t_0) \\ f(t_1) \\ \vdots \\ f(t_N) \end{pmatrix}, \qquad \overrightarrow{\mathbf{f'(t)}} = \begin{pmatrix} f'(t_0) \\ f'(t_1) \\ \vdots \\ f'(t_N) \end{pmatrix}. \quad \text{(A20)}$$

The matrix of the second-order differential operator is defined as $\mathbf{D}_2 \equiv \mathbf{D}^2$.

Then we can build the discretization scheme of Eq. (A3),

$$a_1(t_i)\sum_{j=0}^N (\mathbf{D}_2)_{ij}\tilde{A}_E(t_j) + a_2(t_i)\sum_{j=0}^N \mathbf{D}_{ij}\tilde{A}_E(t_j)$$
$$+ a_3(t_i)\tilde{A}_E(t_i)\sum_{j=0}^N \mathbf{D}_{ij}\tilde{A}_E(t_j) + a_4(t_i)\left[\sum_{j=0}^N \mathbf{D}_{ij}\tilde{A}_E(t_j)\right]^2$$
$$+ a_5(t_i)\tilde{A}_E(t_i) + a_6(t_i)\tilde{A}_E(t_i)^2 + a_7(t_i) = 0 \quad \text{(A21)}$$

with $0 \leq i \leq N$. For $\tilde{f}, \tilde{A}_t, \tilde{\phi}, \tilde{\chi}$, they satisfy the boundary conditions (A11)–(A16), which now turn into

$$\tilde{f}(t_0) - 1 = 0, \tag{A22}$$

$$\tilde{f}(t_N) = 0, \tag{A23}$$

$$\tilde{A}_t(t_0) - \mu_B = 0, \tag{A24}$$

$$\tilde{A}_t(t_N) = 0, \tag{A25}$$

$$\tilde{\phi}(t_0) - p_1 z_h = 0, \tag{A26}$$

$$\tilde{\chi}(t_0) - \zeta m_q z_h = 0. \tag{A27}$$

Hence, the discretized equations for $\tilde{f}$ and $\tilde{A}_t$ should take values from $i \in [1, N-1]$, while the discretized equations for $\tilde{\phi}$ and $\tilde{\chi}$ take values from $i \in [1, N]$. Note that the IR boundary conditions of $\tilde{\phi}$ and $\tilde{\chi}$ are natural boundary conditions which are satisfied implicitly in the equations of motion after discretized.

Then putting the discretized equations and boundary conditions together, we have in total $5(N + 1)$ equations which can be solved numerically to obtain the values of $\tilde{f}(t_i), \tilde{A}_E(t_i), \tilde{A}_t(t_i), \tilde{\phi}(t_i)$, and $\tilde{\chi}(t_i), (0 \leq i \leq N)$. For more details about the spectral collocation method, one can refer to [114,115].

[1] Y. Aoki, G. Endrodi, Z. Fodor, S. D. Katz, and K. K. Szabo, Nature (London) **443**, 675 (2006).
[2] A. Bazavov et al., Phys. Rev. D **85**, 054503 (2012).
[3] T. Bhattacharya et al., Phys. Rev. Lett. **113**, 082001 (2014).
[4] M. G. Alford, A. Schmitt, K. Rajagopal, and T. Schäfer, Rev. Mod. Phys. **80**, 1455 (2008).
[5] E. Laermann and O. Philipsen, Annu. Rev. Nucl. Part. Sci. **53**, 163 (2003).
[6] K. Fukushima and C. Sasaki, Prog. Part. Nucl. Phys. **72**, 99 (2013).
[7] C. S. Fischer, Phys. Rev. Lett. **103**, 052003 (2009).
[8] J. Braun, L. M. Haas, F. Marhauser, and J. M. Pawlowski, Phys. Rev. Lett. **106**, 022002 (2011).
[9] S.-x. Qin, L. Chang, H. Chen, Y.-x. Liu, and C. D. Roberts, Phys. Rev. Lett. **106**, 172301 (2011).
[10] D. T. Son and M. A. Stephanov, Phys. Rev. Lett. **86**, 592 (2001).
[11] C. Ratti, M. A. Thaler, and W. Weise, Phys. Rev. D **73**, 014019 (2006).
[12] B.-J. Schaefer, J. M. Pawlowski, and J. Wambach, Phys. Rev. D **76**, 074023 (2007).
[13] C. R. Allton, S. Ejiri, S. J. Hands, O. Kaczmarek, F. Karsch, E. Laermann, C. Schmidt, and L. Scorzato, Phys. Rev. D **66**, 074507 (2002).
[14] D. Everett et al. (JETSCAPE Collaboration), Phys. Rev. Lett. **126**, 242301 (2021).
[15] S. Borsányi, Z. Fodor, J. N. Guenther, R. Kara, S. D. Katz, P. Parotto, A. Pásztor, C. Ratti, and K. K. Szabó, Phys. Rev. Lett. **126**, 232001 (2021).
[16] J. M. Maldacena, Int. J. Theor. Phys. **38**, 1113 (1999); Adv. Theor. Math. Phys. **2**, 231 (1998).
[17] S. S. Gubser, I. R. Klebanov, and A. M. Polyakov, Phys. Lett. B **428**, 105 (1998).
[18] E. Witten, Adv. Theor. Math. Phys. **2**, 253 (1998).
[19] M. Kruczenski, D. Mateos, R. C. Myers, and D. J. Winters, J. High Energy Phys. 05 (2004) 041.
[20] T. Sakai and S. Sugimoto, Prog. Theor. Phys. **113**, 843 (2005).
[21] T. Sakai and S. Sugimoto, Prog. Theor. Phys. **114**, 1083 (2005).

[22] G. F. de Teramond and S. J. Brodsky, Phys. Rev. Lett. **94**, 201601 (2005).
[23] L. Da Rold and A. Pomarol, Nucl. Phys. **B721**, 79 (2005).
[24] J. Erlich, E. Katz, D. T. Son, and M. A. Stephanov, Phys. Rev. Lett. **95**, 261602 (2005).
[25] A. Karch, E. Katz, D. T. Son, and M. A. Stephanov, Phys. Rev. D **74**, 015005 (2006).
[26] C. Csaki and M. Reece, J. High Energy Phys. 05 (2007) 062.
[27] A. Cherman, T. D. Cohen, and E. S. Werbos, Phys. Rev. C **79**, 045203 (2009).
[28] M. Fujita, K. Fukushima, T. Misumi, and M. Murata, Phys. Rev. D **80**, 035001 (2009).
[29] M. Fujita, T. Kikuchi, K. Fukushima, T. Misumi, and M. Murata, Phys. Rev. D **81**, 065024 (2010).
[30] P. Colangelo, F. Giannuzzi, and S. Nicotri, Phys. Rev. D **80**, 094019 (2009).
[31] P. Colangelo, F. Giannuzzi, S. Nicotri, and V. Tangorra, Eur. Phys. J. C **72**, 2096 (2012).
[32] D. Li, M. Huang, and Q.-S. Yan, Eur. Phys. J. C **73**, 2615 (2013).
[33] D. Li and M. Huang, J. High Energy Phys. 11 (2013) 088.
[34] E. V. Shuryak, Nucl. Phys. **A750**, 64 (2005).
[35] S. J. Brodsky, G. F. de Teramond, H. G. Dosch, and J. Erlich, Phys. Rep. **584**, 1 (2015).
[36] M. J. Tannenbaum, Rep. Prog. Phys. **69**, 2005 (2006).
[37] G. Policastro, D. T. Son, and A. O. Starinets, Phys. Rev. Lett. **87**, 081601 (2001).
[38] R.-G. Cai, Z.-Y. Nie, N. Ohta, and Y.-W. Sun, Phys. Rev. D **79**, 066004 (2009).
[39] R.-G. Cai, Z.-Y. Nie, and Y.-W. Sun, Phys. Rev. D **78**, 126007 (2008).
[40] S.-J. Sin and I. Zahed, Phys. Lett. B **608**, 265 (2005).
[41] E. Shuryak, S.-J. Sin, and I. Zahed, J. Korean Phys. Soc. **50**, 384 (2007).
[42] H. Nastase, arXiv:hep-th/0501068.
[43] S. Nakamura and S.-J. Sin, J. High Energy Phys. 09 (2006) 020.
[44] S.-J. Sin, S. Nakamura, and S. P. Kim, J. High Energy Phys. 12 (2006) 075.

[45] R. A. Janik and R. B. Peschanski, Phys. Rev. D **73**, 045013 (2006).

[46] C. P. Herzog, A. Karch, P. Kovtun, C. Kozcaz, and L. G. Yaffe, J. High Energy Phys. 07 (2006) 013.

[47] U. Gursoy and E. Kiritsis, J. High Energy Phys. 02 (2008) 032.

[48] U. Gursoy, E. Kiritsis, and F. Nitti, J. High Energy Phys. 02 (2008) 019.

[49] T. Gherghetta, J. I. Kapusta, and T. M. Kelley, Phys. Rev. D **79**, 076003 (2009).

[50] T. M. Kelley, S. P. Bartz, and J. I. Kapusta, Phys. Rev. D **83**, 016002 (2011).

[51] Y.-Q. Sui, Y.-L. Wu, Z.-F. Xie, and Y.-B. Yang, Phys. Rev. D **81**, 014024 (2010).

[52] Y.-Q. Sui, Y.-L. Wu, and Y.-B. Yang, Phys. Rev. D **83**, 065030 (2011).

[53] L.-X. Cui, Z. Fang, and Y.-L. Wu, Eur. Phys. J. C **76**, 22 (2016).

[54] L.-X. Cui, Z. Fang, and Y.-L. Wu, Chin. Phys. C **40**, 063101 (2016).

[55] Z. Fang, D. Li, and Y.-L. Wu, Phys. Lett. B **754**, 343 (2016).

[56] Z. Fang, Phys. Rev. D **94**, 074017 (2016).

[57] C. P. Herzog, Phys. Rev. Lett. **98**, 091601 (2007).

[58] D. Li, J. Liao, and M. Huang, Phys. Rev. D **89**, 126006 (2014).

[59] D. Li, S. He, and M. Huang, J. High Energy Phys. 06 (2015) 046.

[60] Z. Fang, Phys. Lett. B **758**, 1 (2016).

[61] N. Evans, C. Miller, and M. Scott, Phys. Rev. D **94**, 074034 (2016).

[62] K. A. Mamo, Phys. Rev. D **94**, 041901 (2016).

[63] D. Dudal and S. Mahapatra, J. High Energy Phys. 04 (2017) 031.

[64] D. Dudal and T. G. Mertens, Phys. Rev. D **97**, 054035 (2018).

[65] A. Ballon-Bayona, M. Ihl, J. P. Shock, and D. Zoakos, J. High Energy Phys. 10 (**2017**) 038.

[66] J. Chen, S. He, M. Huang, and D. Li, J. High Energy Phys. 01 (2019) 165.

[67] K. Chelabi, Z. Fang, M. Huang, D. Li, and Y.-L. Wu, J. High Energy Phys. 04 (**2016**) 036.

[68] K. Chelabi, Z. Fang, M. Huang, D. Li, and Y.-L. Wu, Phys. Rev. D **93**, 101901 (2016).

[69] Z. Fang, Y.-L. Wu, and L. Zhang, Phys. Lett. B **762**, 86 (2016).

[70] D. Li and M. Huang, J. High Energy Phys. 02 (2017) 042.

[71] S. P. Bartz and T. Jacobson, Phys. Rev. C **97**, 044908 (2018).

[72] S. P. Bartz and T. Jacobson, Phys. Rev. D **94**, 075022 (2016).

[73] Z. Fang, Y.-L. Wu, and L. Zhang, Phys. Rev. D **98**, 114003 (2018).

[74] Z. Fang, Y.-L. Wu, and L. Zhang, Phys. Rev. D **99**, 034028 (2019).

[75] Z. Fang, Y.-L. Wu, and L. Zhang, Phys. Rev. D **100**, 054008 (2019).

[76] S. S. Gubser, A. Nellore, S. S. Pufu, and F. D. Rocha, Phys. Rev. Lett. **101**, 131601 (2008).

[77] S. S. Gubser and A. Nellore, Phys. Rev. D **78**, 086007 (2008).

[78] U. Gursoy, E. Kiritsis, L. Mazzanti, and F. Nitti, Phys. Rev. Lett. **101**, 181601 (2008).

[79] J. Noronha, Phys. Rev. D **81**, 045011 (2010).

[80] S. I. Finazzo and J. Noronha, Phys. Rev. D **89**, 106008 (2014).

[81] S. I. Finazzo and J. Noronha, Phys. Rev. D **90**, 115028 (2014).

[82] O. Andreev, Phys. Rev. Lett. **102**, 212001 (2009).

[83] R. Yaresko and B. Kampfer, Phys. Lett. B **747**, 36 (2015).

[84] R. Yaresko, J. Knaute, and B. Kämpfer, Eur. Phys. J. C **75**, 295 (2015).

[85] P. Colangelo, F. Giannuzzi, and S. Nicotri, Phys. Rev. D **83**, 035015 (2011).

[86] D. Li, S. He, M. Huang, and Q.-S. Yan, J. High Energy Phys. 09 (2011) 041.

[87] S. He, S.-Y. Wu, Y. Yang, and P.-H. Yuan, J. High Energy Phys. 04 (2013) 093.

[88] Y. Yang and P.-H. Yuan, J. High Energy Phys. 11 (2014) 149.

[89] Z. Fang, S. He, and D. Li, Nucl. Phys. **B907**, 187 (2016).

[90] R. Rougemont, R. Critelli, J. Noronha-Hostler, J. Noronha, and C. Ratti, Phys. Rev. D **96**, 014032 (2017).

[91] Z. Li, Y. Chen, D. Li, and M. Huang, Chin. Phys. C **42**, 013103 (2018).

[92] R. Zöllner and B. Kämpfer, Eur. Phys. J. Plus **135**, 304 (2020).

[93] X. Chen, D. Li, and M. Huang, Chin. Phys. C **43**, 023105 (2019).

[94] O. DeWolfe, S. S. Gubser, and C. Rosen, Phys. Rev. D **83**, 086005 (2011).

[95] O. DeWolfe, S. S. Gubser, and C. Rosen, Phys. Rev. D **84**, 126014 (2011).

[96] R. Critelli, J. Noronha, J. Noronha-Hostler, I. Portillo, C. Ratti, and R. Rougemont, Phys. Rev. D **96**, 096026 (2017).

[97] M. Jarvinen and E. Kiritsis, J. High Energy Phys. 03 (2012) 002.

[98] T. Alho, M. Järvinen, K. Kajantie, E. Kiritsis, and K. Tuominen, J. High Energy Phys. 01 (2013) 093.

[99] T. Alho, M. Jarvinen, K. Kajantie, E. Kiritsis, C. Rosen, and K. Tuominen, J. High Energy Phys. 04 (2014) 124; 02 (2015) 33(E).

[100] Z. Fang and Y.-L. Wu, Chin. Phys. C **44**, 103101 (2020).

[101] Y.-Y. Li, X.-L. Liu, X.-Y. Liu, and Z. Fang, Phys. Rev. D **105**, 034019 (2022).

[102] R.-G. Cai, S. He, L. Li, and Y.-X. Wang, Phys. Rev. D **106**, L121902 (2022).

[103] G. Boyd, J. Engels, F. Karsch, E. Laermann, C. Legeland, M. Lutgemeier, and B. Petersson, Nucl. Phys. **B469**, 419 (1996).

[104] K. Fukushima and T. Hatsuda, Rep. Prog. Phys. **74**, 014001 (2011).

[105] X. Chen, D. Li, D. Hou, and M. Huang, J. High Energy Phys. 03 (2020) 073.

[106] C. R. Allton, S. Ejiri, S. J. Hands, O. Kaczmarek, F. Karsch, E. Laermann, and C. Schmidt, Phys. Rev. D **68**, 014507 (2003).

[107] F. Karsch, Nucl. Phys. **A698**, 199 (2002).

[108] C. R. Allton, M. Doring, S. Ejiri, S. J. Hands, O. Kaczmarek, F. Karsch, E. Laermann, and K. Redlich, Phys. Rev. D **71**, 054508 (2005).

[109] T. Sasaki, Y. Sakai, H. Kouno, and M. Yahiro, Phys. Rev. D **82**, 116004 (2010).

[110] W.-j. Fu, J. M. Pawlowski, and F. Rennecke, Phys. Rev. D **101**, 054032 (2020).

[111] F. Gao and J. M. Pawlowski, Phys. Rev. D **102**, 034027 (2020).

[112] F. Gao and Y.-x. Liu, Phys. Rev. D **94**, 076009 (2016).

[113] Y.-Q. Zhao, S. He, D. Hou, L. Li, and Z. Li, arXiv:2310.13432.

[114] J. Shen, T. Tang, and L.-L. Wang, *Spectral Methods: Algorithms, Analysis and Applications* (Springer Science & Business Media, Berlin, Heidelberg, 2011).

[115] Y. H. Yin, A. Sun, and T. J. Wang, Spectral collocation methods for a class of nonlinear singular boundary value problems, in *Proceedings of the 2013 International Conference on Advanced Mechatronic Systems* (IEEE, Luoyang, China, 2013), pp. 609–612.